Supplementary information for

Accelerating metal nanoparticle exsolution by exploiting tolerance factor of perovskite stannate

Yujeong Lee[1), 2), 3), #], Daseob Yoon[1), #], Yeon-Seo Nam[1), #], Sangbae Yu[1)], Chaesung Lim[2)], Hyeji Sim[1)], Yunkyu Park[1)], Jeong Woo Han[2),3),*], Si-Young Choi[1),*], and Junwoo Son[2),3),*]

[1)] Department of Materials Science and Engineering, Pohang University of Science and Technology (POSTECH), Pohang 37673, Republic of Korea

[2)] Research Institute of Advanced Materials, Seoul National University, Seoul 08826, Republic of Korea

[3)] Department of Materials Science and Engineering, Seoul National University, Seoul 08826, Republic of Korea

[#] These authors contributed equally to this work.

* junuson@snu.ac.kr; youngchoi@postech.ac.kr; jwhan98@snu.ac.kr;

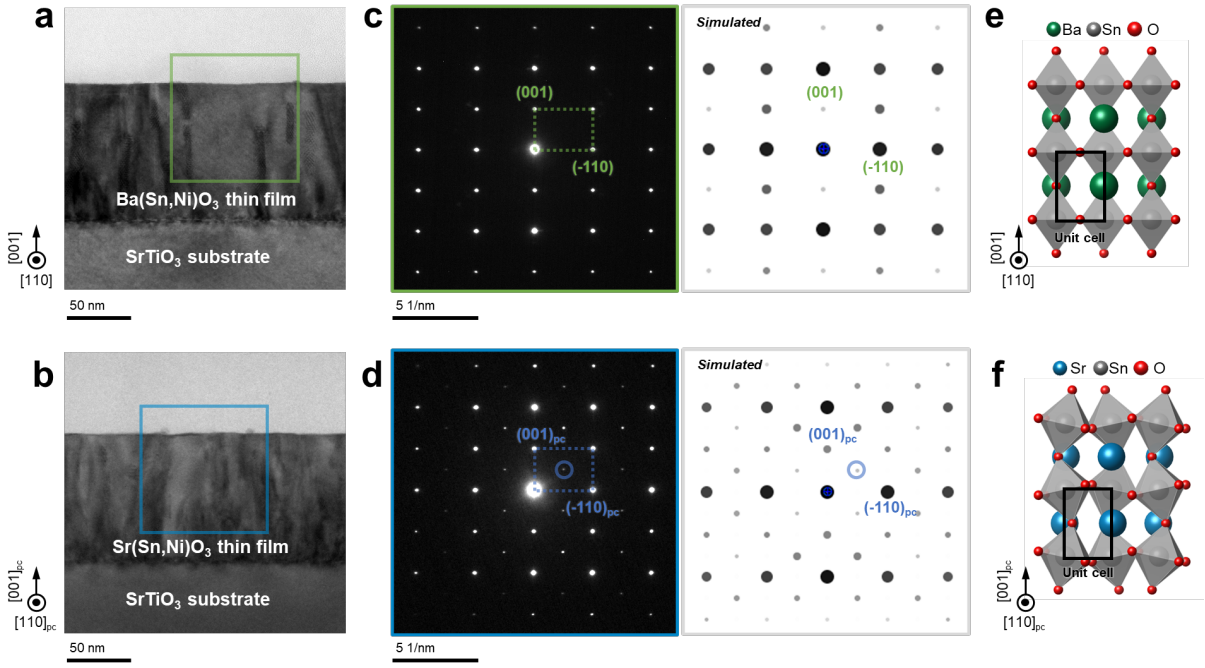

Figure S1 | The crystal structure of $Ba(Sn,Ni)O_3$ [$Pm\bar{3}m$] and $Sr(Sn,Ni)O_3$ [Pnma] using transmission electron microscopy. a, The low magnification image of $Ba_{0.9}Sn_{0.9}Ni_{0.1}O_{3-\delta}$ (BSNO) and **b,** $Sr_{0.9}Sn_{0.9}Ni_{0.1}O_{3-\delta}$ (SSNO) film with ~100 nm thickness on $SrTiO_3$ substrate along with [110] and $[110]_{pc}$ zone axis. **c,** The experimental diffraction patterns of BSNO (green square marked in **Fig. S1a**) and **d,** SSNO thin film (blue square marked in **Fig. S1b**), with simulated diffraction patterns. **e,** The crystal structure of BSNO and **f,** SSNO marked with black squares indicates the unit cell.

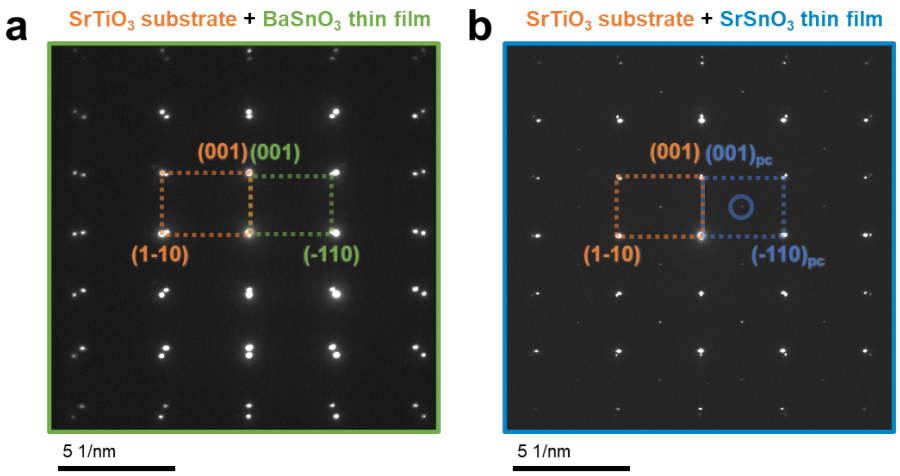

Figure S2 | Strain relaxation between the BSNO (SSNO) epitaxial thin film and $SrTiO_3$ substrate. a, The electron diffraction patterns of BSNO and **b,** SSNO thin film with the $SrTiO_3$ substrate, respectively. Spot splitting due to the lattice parameter difference between BSNO(SSNO) films and $SrTiO_3$ substrate.

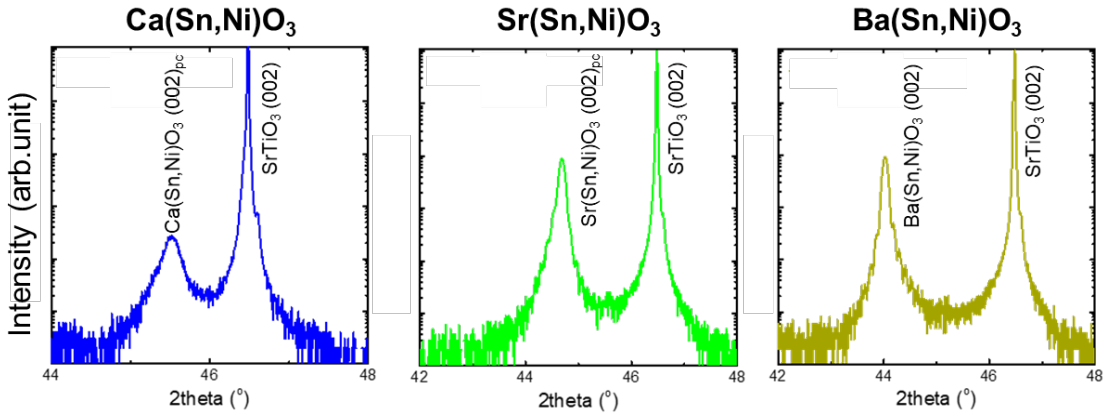

Figure S3 | X-ray diffraction of A(Sn,Ni)O$_3$ (A = Ca, Sr, Ba) thin films after exsolution process. θ-2θ scan of (001)-oriented Ca(Sn,Ni)O$_3$, Sr(Sn,Ni)O$_3$, and Ba(Sn,Ni)O$_3$ epitaxial thin films on SrTiO$_3$ single-crystal substrates. After exsolution treatment, no secondary phase peak was observed in x-ray diffraction, which indicates that perovskite stannate framework was maintained even after thermal annealing process.

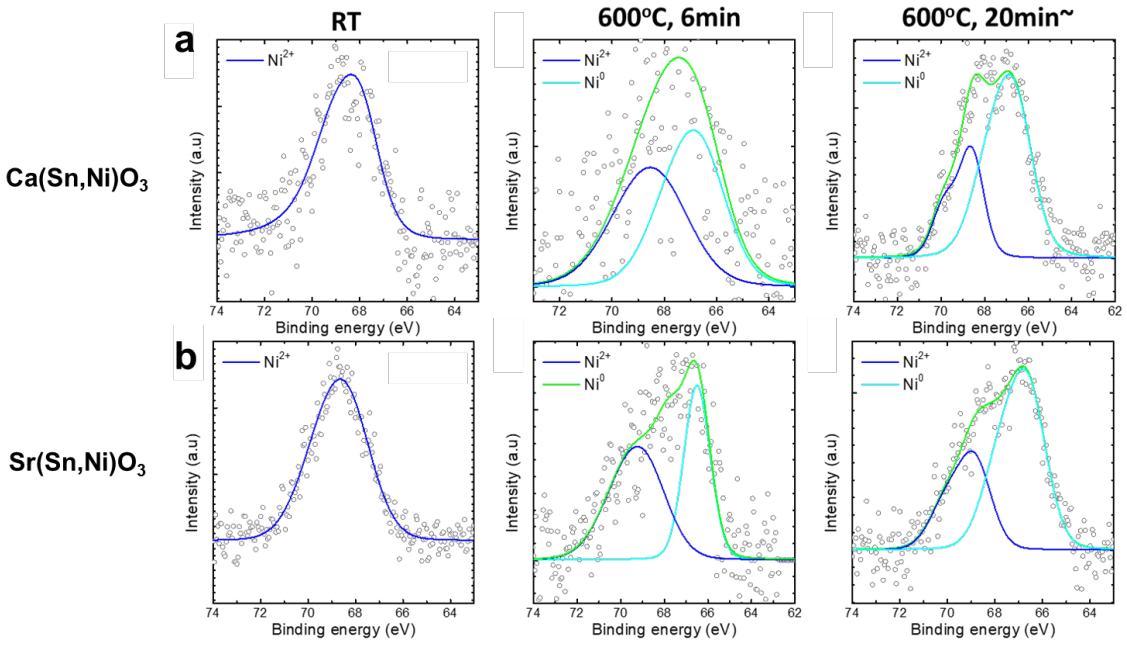

Figure S4 | *In situ* APXPS Ni 3*p* spectra of Ca(Sn, Ni)O_3 and Sr(Sn, Ni)O_3 matrix as a function of annealing time during exsolution. a, Time-dependent Ni 3*p* spectra of Ca(Sn,Ni)O_3 and **b,** Sr(Sn,Ni)O_3 at different annealing condition: room temperature, 600°C (maintained for 6 min), 600°C (maintained for 20 min). Note that Ni 3*p* spectra were deconvoluted into Ni^{2+} 3*p* and Ni^0 3*p* peaks for quantitative analysis.

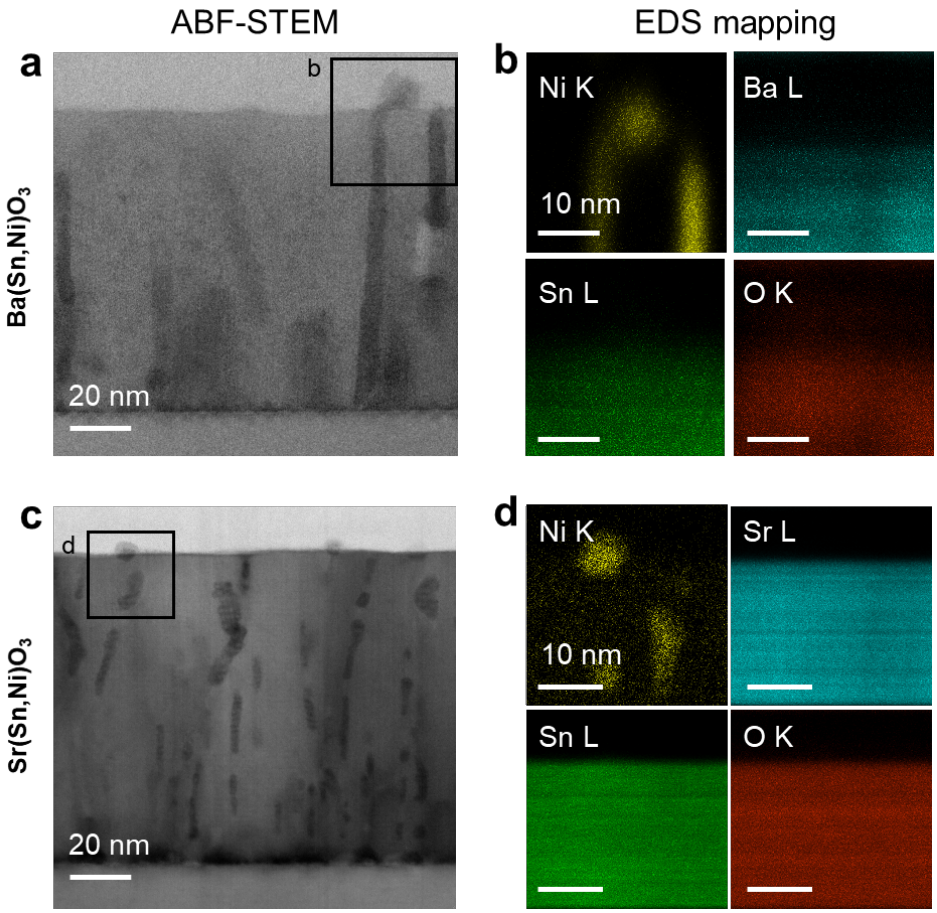

Figure S5 | STEM-EDS mapping of exsolved particles. a, Cross-sectional ABF-STEM image depicting an annealed BSNO film. **b,** EDS elemental map highlighting the distribution of Ni, Ba, Sn and O (located within the black square in **Fig S5a**). **c,** Cross-sectional ABF-STEM image illustrating an annealed SSNO film. **d,** EDS elemental map showcasing the spatial distribution of Ni, Sr, Sn and O (enclosed within the black square in **Fig S5c**). Both ABF images along with the corresponding EDS mapping images, with a zone axis at [110] and $[110]_{pc}$.

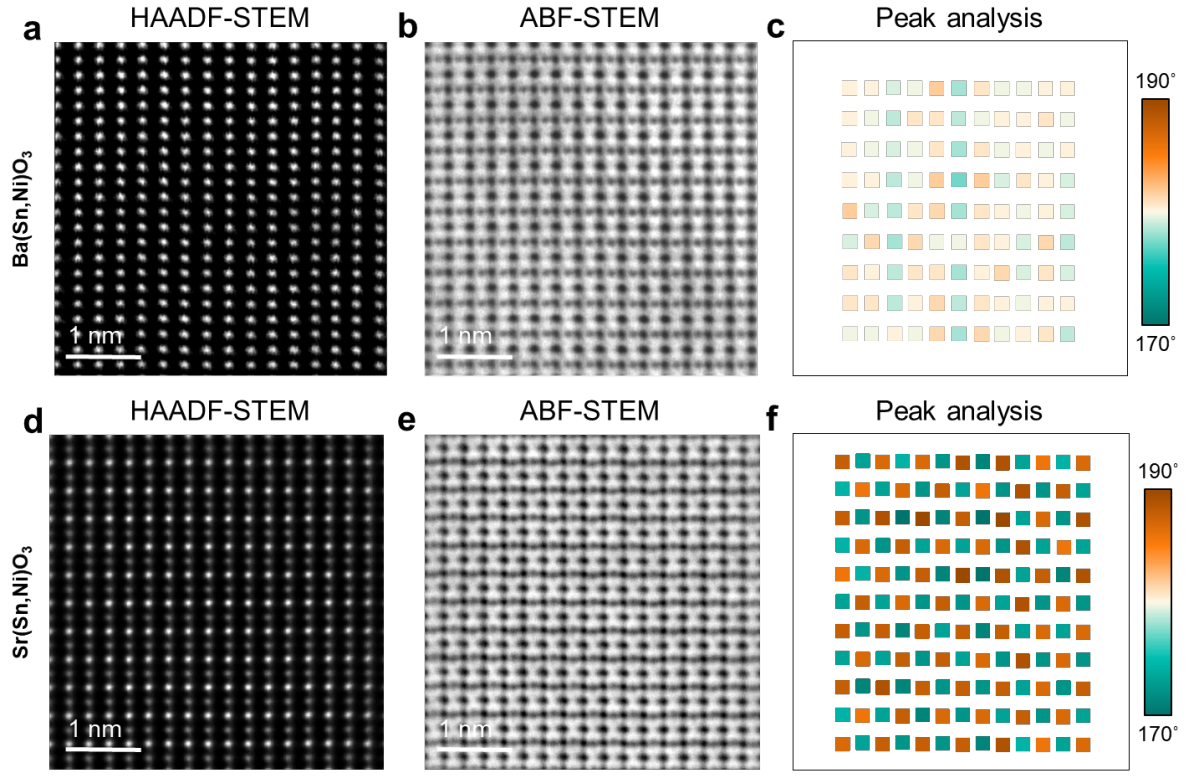

Figure S6 | Oxygen tilting angles of BSNO and SSNO thin films. a, HAADF and **b,** ABF images of BSNO, respectively, showing the Sn-O-Sn angle within their lattice structures. **c,** The colored boxes in the graph represent the distribution and variation of the Sn-O-Sn tilting angle in the BSNO thin film. **d,** HAADF and **e,** ABF images of SSNO, respectively, showing the Sn-O-Sn angle within their lattice structures. **f,** The colored boxes in the graph illustrate the distribution and variation of the Sn-O-Sn tilting angle in SSNO thin film. The data presented in the graph depict the distribution of Sn-O-Sn angle in both BSNO and SSNO thin films.

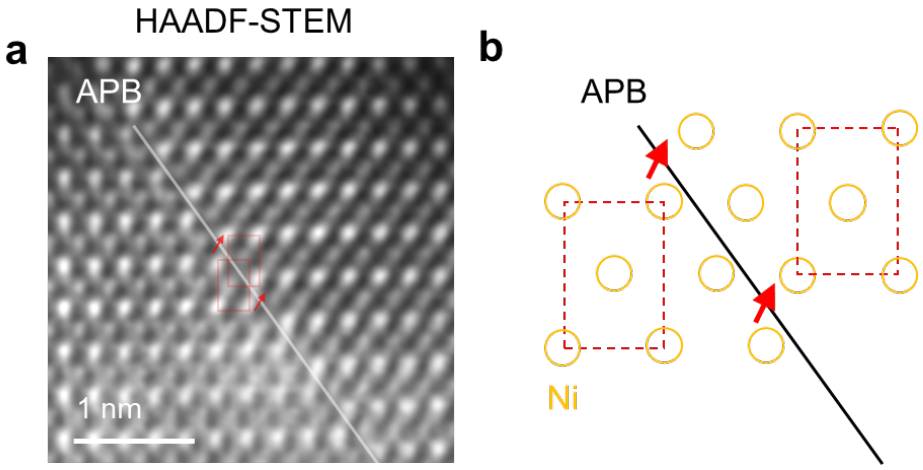

Figure S7 | Antiphase boundary in Ni particle on SSNO thin film. a, HAADF-STEM image highlighting antiphase boundaries (APB) in the Ni particle on the SSNO surface. The white line indicates the APB and the red line denotes the displaced Ni atoms. **b,** Schematic model illustrating the configuration of the APB.

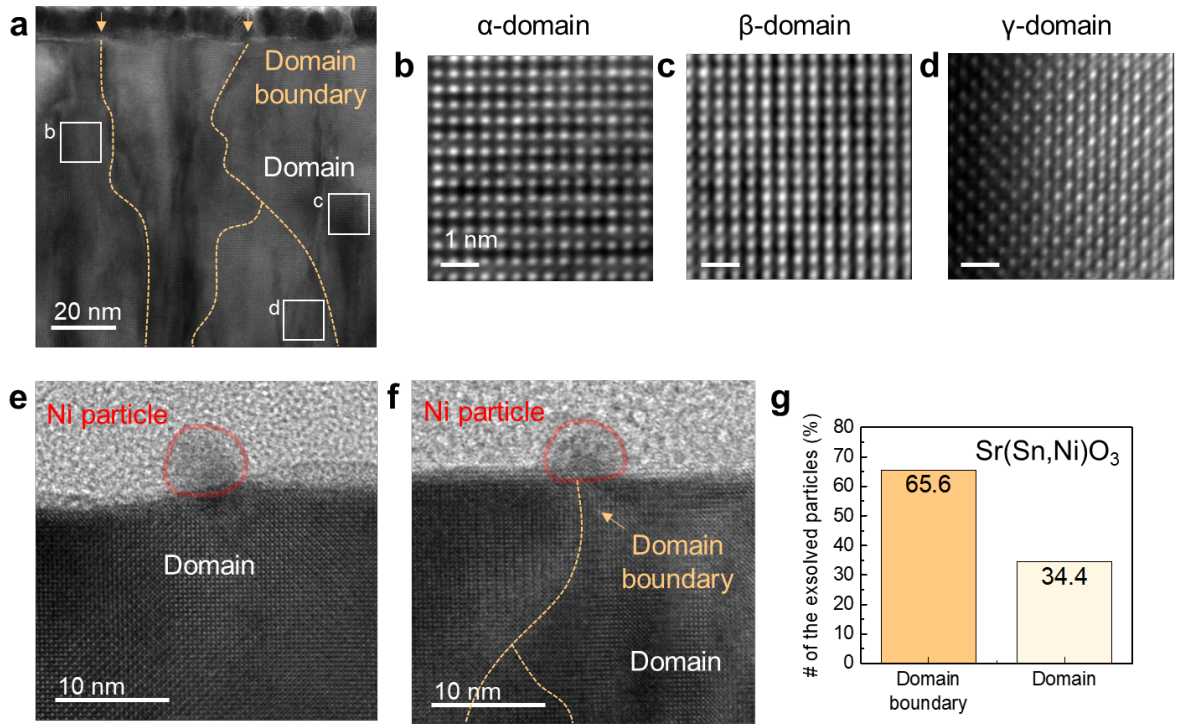

Figure S8 | Atomic-scale analysis of exsolved Ni nanoparticles on domain boundaries in the perovskite alkaline stannate SSNO matrix after exsolution. a, Cross-sectional HRTEM image of as-grown SSNO film. Note that the low-magnification image shows the oriented domains and domain boundaries (indicated by orange dotted lines) in the SSNO epitaxial film. **b,** High magnified images of the oriented domains: α-domain, **c,** β-domain, and **d,** γ-domain. **e,** HRTEM image of the Ni nanoparticle on the domain and **f**, the domain boundary in the annealed SSNO film. The exsolved Ni particles are marked by pale red lines. **g,** The number of the exsolved Ni nanoparticles on domains and domain boundaries extracted from HRTEM images. The total number of Ni NPs was 26.

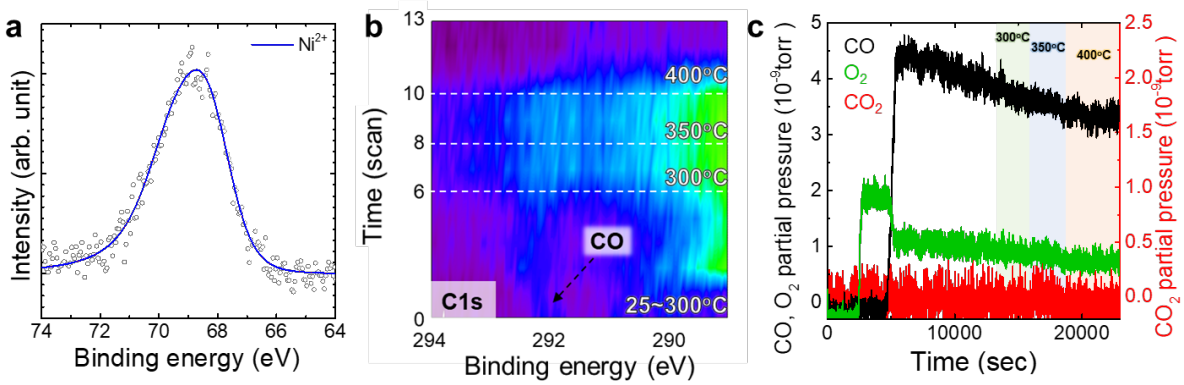

Figure S9 | *In situ* CO oxidation of as-grown LCSNO matrix. a, Ni 3p spectrum of as-grown LCSNO epitaxial thin films without exsolved Ni nanoparticles. **b,** As-grown LCSNO during heating (25 °C → 400 °C) under CO and O_2 gas flows. The peak assigned to the CO gas phase (E_b = 291.81 eV) shifted to lower binding energy under heating. The conversion of CO to CO_2 was carried out under 1.02 mbar CO gas and 1.06 mbar O_2 gas. **c,** Chemical composition of the reactant and product gas during CO oxidation using RGA. The partial pressure of CO_2 gas remained almost constant under the CO and O_2 gas reaction.

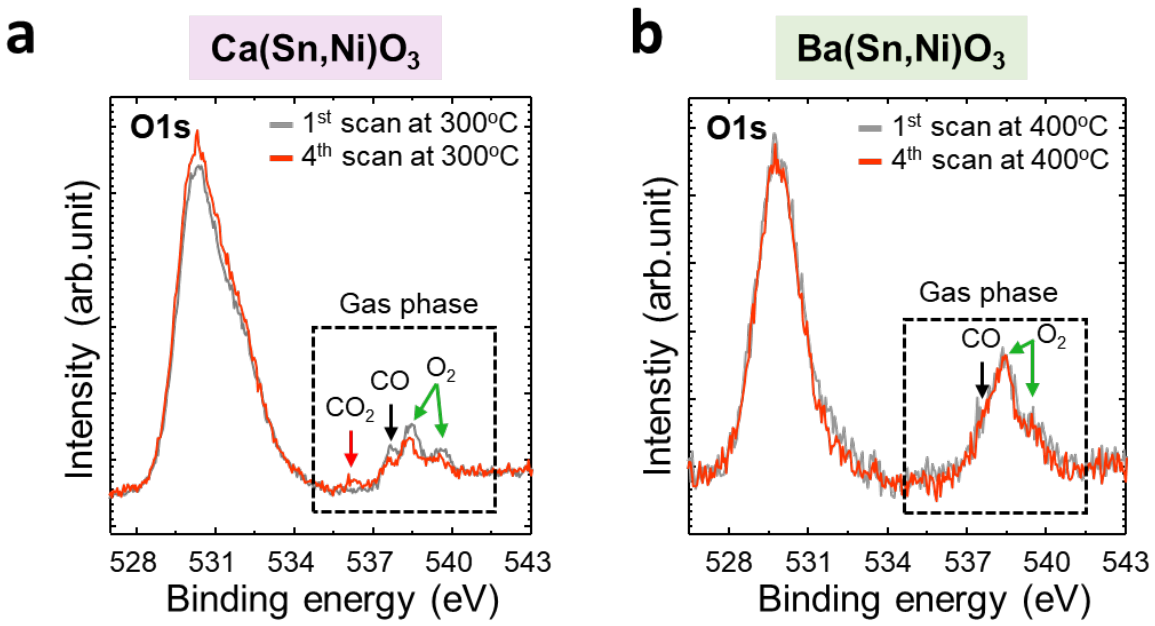

Figure S10 | *In situ* APXPS O 1*s* spectra of Ni-exsolved LCSNO and LBSNO films during CO oxidation reaction. a, The O 1*s* spectra of Ni-exsolved LCSNO films at 300°C and **b,** Ni-exsolved LBSNO at 400°C during CO oxidation reaction. Note that gas phase peak related to CO_2 obviously evolved in Ni-exsolved LCSNO films at the expense of CO and O_2 gas phase peaks (a).